Anisotropic suppression of octahedral breathing distortion with the fully strained $BaBiO_3/BaCeO_3$ heterointerface

Han Gyeol Lee, Rokyeon Kim, Jinkwon Kim, Minu Kim, Tae Heon Kim, Shinbuhm Lee, and Tae Won Noh

Citation: APL Materials **6**, 016107 (2018); doi: 10.1063/1.5010825
View online: https://doi.org/10.1063/1.5010825
View Table of Contents: http://aip.scitation.org/toc/apm/6/1
Published by the American Institute of Physics

Anisotropic suppression of octahedral breathing distortion with the fully strained $BaBiO_3/BaCeO_3$ heterointerface

Han Gyeol Lee,[1,2] Rokyeon Kim,[1,2] Jinkwon Kim,[1,2] Minu Kim,[1,2] Tae Heon Kim,[3] Shinbuhm Lee,[4,a] and Tae Won Noh[1,2,a]

[1]*Center for Correlated Electron Systems, Institute for Basic Science (IBS), Seoul 08826, South Korea*

[2]*Department of Physics and Astronomy, Seoul National University (SNU), Seoul 08826, South Korea*

[3]*Department of Physics, University of Ulsan, Ulsan 44610, South Korea*

[4]*Department of Emerging Materials Science, Daegu Gyeongbuk Institute of Science and Technology, Daegu 42988, South Korea*

(Received 27 October 2017; accepted 3 January 2018; published online 23 January 2018)

While the physiochemical effects of octahedral tilting and rotating distortions have been studied extensively, octahedral breathing distortion (OBD) at heterointerfaces has rarely been explored. Here, we investigated OBD in fully strained $BaBiO_3$ (BBO) epitaxial films by making a new type of oxide heterointerface with non-breathing $BaCeO_3$ epitaxial films. The integration of first-principles calculations with experimental observations of optical spectroscopy revealed that the oxygen displacement modes in BBO became disordered within six unit cells at the heterointerface and the surface. Controlling OBD in perovskite oxide thin films provides a means to exploit emerging material properties. https://doi.org/10.1063/1.5010825

Control of octahedral distortion in perovskite oxide heterostructures has attracted much attention as an emergent route to discover novel multifunctional materials.[1] Perovskite oxides (ABO_3; A = alkali metal, B = transition metal, O = oxygen) have a simple crystallographic structure with corner-sharing BO_6 octahedra surrounded by A-site ions. The octahedra are composed of central B-site transition metal cations coordinated by six oxygen ligands.[2–4] These materials have numerous functionalities, including superconductivity, magnetism, ferroelectricity, and multiferroics.[5–8] Such diverse functionalities of these versatile materials arise from the number of occupied electrons in the B-site ions and structural variation of the BO_6 octahedra, such as size, shape, and connectivity. Recently, there have been extensive studies to control the octahedral connectivity in oxide thin films and heterostructures by epitaxial synthesis.[9–11] To date, most studies have focused on tilting and rotating of the octahedra via strain, interfacial control, and/or having a short-period superlattice.[12–15]

$BaBiO_3$ (BBO) is an intriguing material with characteristic octahedral distortion, namely, an alternating octahedral breathing distortion (OBD). A neutron diffraction study showed that there are two distinct sites for Bi ions.[16] As shown in Fig. 1(a), two neighboring BO_6 octahedra have alternating OBD: one swelling and the other collapsing. This alternating size variation can be arranged in a three-dimensional (3D) checkerboard pattern without altering the cubic point symmetry, i.e., A_{1g} symmetry. In this 3D arrangement, we can view the OBD in terms of two distinguishable modes of oxygen motions. As schematically displayed in the top areas of Figs. 1(b) and 1(c) (i.e., away from the interface), there will be an oxygen up-down mode in the BaO layer and an oxygen expanding-shrinking mode in the BiO_2 layer, together comprising OBD.

The OBD in BBO generates intriguing emerging material properties. This structural change is accompanied by strong hybridization of Bi-6*s* and O-2*p* orbitals, which affects the Bi covalency

[a]lee.shinbuhm@dgist.ac.kr and twnoh@snu.ac.kr

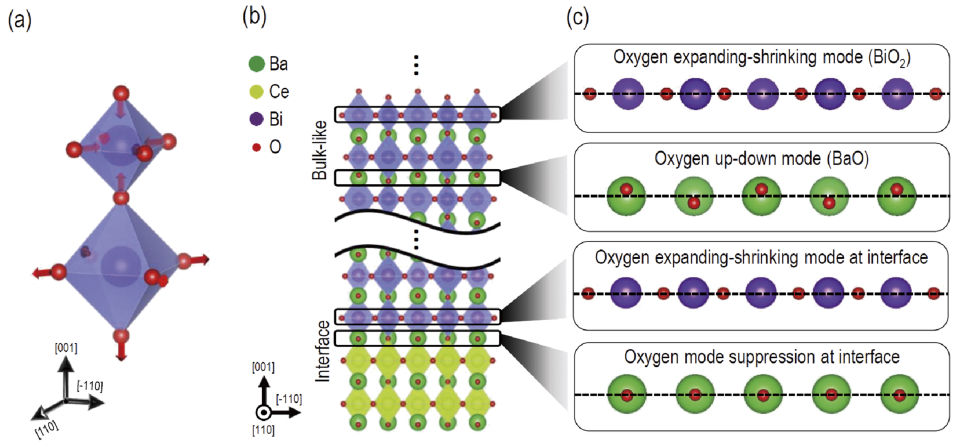

FIG. 1. (a) Schematic diagram of octahedral breathing distortion (OBD) in ABO_3 perovskite oxides. Each arrow indicates the direction of oxygen displacement. Oxygen move inward for a collapsed octahedron and outward for a swollen octahedron. (b) Schematic crystal structures of 6-u.c.-thick $BaBiO_3$ (BBO) films on a (001)-oriented $BaCeO_3$ (BCO) layer. The [110] view is used to clearly show the difference between OBD in BBO and non-breathing octahedra in BCO. The expected oxygen displacement is drawn in an exaggerated scale. (c) Zoomed view of the oxygen displacement mode of the BaO layer and BiO_2 layer of BBO. In the bulk-like region, oxygen octahedra show up-down distortion in the BaO layer and expanding-shrinking distortion in the BiO_2 layer. However, near the heterointerface, the oxygen up-down mode is suppressed, while the expanding-shrinking mode remains.

as alternative $Bi^{4+\delta}$ and $Bi^{4-\delta}$, forming a charge density wave (CDW).[17] It is widely accepted that the CDW induces a strong absorption peak around 2.0 eV in BBO,[18,19] leading to the insulating property of BBO. In chemically doped BBO, the suppression of OBD and the associated CDW can induce an insulator-to-superconductor transition with critical temperature as high as 34 K.[18,20–22] Likewise, OBD-induced properties also exist in other perovskite materials, including the metal–insulator transition of nickelates.[23,24]

However, the OBD in BBO raises fundamental questions for high-quality ultrathin film fabrication. Note that most commercially available oxide substrates do not have OBD. When we try to grow a BBO film on a substrate without OBD, there should exist a strong mismatch in atomic arrangements at the interface of the heterostructure. In most previous studies on perovskite oxide heterostructures, the size of the BO_6 units was treated as nearly rigid; thus, structural mismatch at the interface results in tilt and/or rotations of the BO_6 units.[2,15] If the large and small sizes of the BiO_6 octahedra cannot be varied, the atomic arrangements of the BBO film is not readily compatible with those of the substrate. Such incompatibilities should be resolved to obtain high-quality BBO thin films. Therefore, it is scientifically and practically important to understand how the OBD of fully strained BBO film becomes relaxed near the heterointerface with non-breathing material (i.e., without OBD).

Here we grew BBO epitaxial films commensurately on non-breathing $BaCeO_3$ (BCO) layers using a pulsed laser deposition technique (see supplementary material, Figs. S1 and S2). The lattice constant of BCO ($a = 4.397$ Å in bulk) is similar to that of BBO ($a = 4.371$ Å), allowing us to grow a fully strained BBO film with a commensurate interface.[25] It should be noted that we used a $BaZrO_3$ (BZO) buffer layer to reduce the large lattice mismatch of 11.5% between the BCO layer and a $SrTiO_3$ (STO) substrate. Lee *et al.*[25] showed that the BZO buffer accommodates huge lattice mismatch with the lattice relaxation due to the formation of misfit dislocations at the interface, providing a proper sublayer to grow a BCO layer. Hydrofluoric acid-etched (001)-oriented STO substrates were put into a vacuum chamber (base pressure: 10^{-9} Torr; Pascal, Osaka, Japan) and pre-annealed at 950 °C for 30 min in a 5×10^{-6}-Torr oxygen environment. This process has been widely used to obtain a TiO_2-terminated atomically flat step-terraced surface.[26] The oxygen partial pressure was then increased to 100 mTorr. We grew the BZO layer at 500 °C, the BCO layer at 750 °C, and finally the BBO layer at 500 °C. Each target was ablated by a KrF excimer laser (wavelength $\lambda = 248$ nm; Coherent, Santa Clara, CA, USA) at a laser fluence of 0.6 J/cm^2. After growth, the crystal structure was

characterized by high-resolution X-ray diffraction (XRD, λ = 1.540 Å; Bruker, Karlsruhe, Germany). Spectroscopic characterization was performed with a Raman microscope (Renishaw, New Mills, UK) and spectroscopic ellipsometer (Woollam, Lincoln, NE, USA) to investigate the phonon modes and electronic structure, respectively.

We investigated the structural evolution of OBD by measuring the Raman response as a function of BBO thickness, as shown in Fig. 2(a). It is known that the Raman peak of BBO arises from its A_{1g} symmetric breathing phonon mode,[27] which is characteristically activated at a Raman shift of 565 cm^{-1}. The Raman spectra of BBO were obtained using 633-nm-wavelength laser irradiation (~1.96 eV) to maximize the Raman response via resonance with the strong absorption peak of BBO (~2.0 eV). With the resonance beam, we could obtain a distinctive Raman response from the BBO film, even if the volume of the film is much smaller than that of the substrate. The Raman spectra from different samples were normalized with the intensity of the Raman response which comes from the phonon mode of the STO substrate. A strong Raman response at 565 cm^{-1} and its second harmonic at 1130 cm^{-1} were observed for the 20-u.c.-thick BBO sample. However, with a decrease in BBO film thickness, the Raman response at 565 cm^{-1} was gradually suppressed. Below 6 u.c., the Raman signature at 565 cm^{-1} vanished completely, resulting in a Raman spectrum similar to that of a BCO/BZO/STO sample. This result indicates that the A_{1g} symmetric phonon mode related to OBD should be suppressed at 6 u.c. Above this critical thickness, the OBD-related A_{1g} mode recovers in BBO, although BBO remained fully strained by the underlying BCO layer. If the reduced thickness is the origin of optical signal suppression, the intensity of the optical signal should be linearly proportional to the thickness. However, the trend of suppression is abrupt at a sudden thickness, independent of the linear thickness variation.

The evolution of the OBD-associated CDW feature was also observed in optical conductivity spectra $\sigma_1(\omega)$, as shown in Fig. 2(b). As mentioned earlier, the hybridization of the Bi-6*s* and O-2*p* orbitals, associated with OBD, results in a CDW. This CDW creates a density of states below and above the Fermi level of its electronic band structure, resulting in a strong absorption peak around 2.0 eV.[19,28] Therefore, we investigated the CDW via direct optical transition measurements. As shown by the red line, the 20-u.c.-thick BBO film showed a significant peak at 2.05 eV. Interestingly, the peak gradually becomes weakened with a reduction in BBO film thickness.

The close relationship between suppression of the A_{1g} Raman mode and the CDW absorption peak was clearly displayed in Fig. 2(c). The Raman intensities at 565 cm^{-1}, the characteristic Raman shift for OBD, are plotted as a function of BBO thickness in the upper section. Optical conductivities at 2.05 eV, the characteristic CDW feature, are plotted in the bottom section. These two plots clearly show similar discrete behaviors near 6–8 u.c., as indicated by the red-highlighted

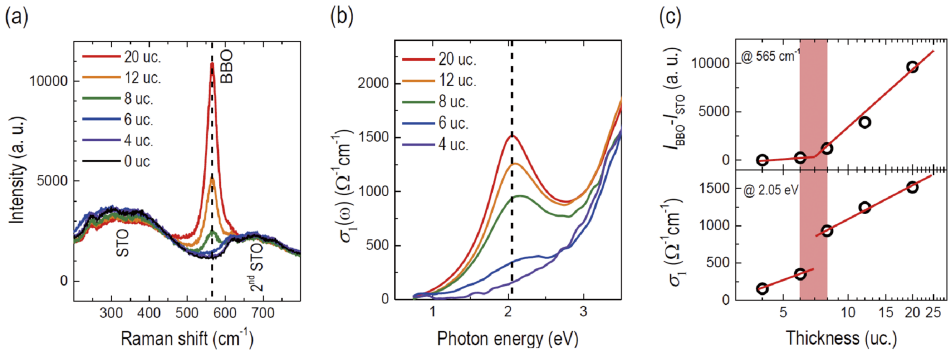

FIG. 2. (a) Raman responses of fully strained BBO with variation of film thickness when the sample is exposed to 633-nm laser irradiation. The first and second harmonics at 565 cm^{-1} and 1130 cm^{-1} are excited due to the oxygen octahedral breathing phonon modes of BBO. With an increase in film thickness, those peaks weaken and eventually disappear for film thicknesses below 6 u.c. (b) Optical conductivity spectra of BBO films with variation in film thickness. The absorption maximum at 2.05 eV comes from direct optical transitions across the OBD-associated charge density wave gap in BBO. With an increase in film thickness, those peaks are weakened and disappear for films less than 6 u.c. in thickness. (c) Summary of the evolution of the Raman intensity values at 565 cm^{-1} and optical conductivity values at 2.05 eV as a function of BBO film thickness. Both values show discontinuity near 6–8 u.c., highlighted in red. Solid lines are guides for the eye.

region. Above the boundary, bulk-like OBD and the associated CDW recover. However, the Raman response of the 6 u.c. sample was completely suppressed, while the $\sigma_1(\omega)$ peak shows a small trace of spectral weight at 6 u.c. The difference between the Raman and $\sigma_1(\omega)$ response may be due to anisotropic suppression of OBD. This possibility will be discussed later in more detail with theoretical calculations.

Transmission electron microscopy (TEM) is the most promising technique for observation of octahedral distortion.[9,12] However, TEM has serious limitations with regard to OBD investigations of BBO films. The crystal structure of BBO is fragile and easily destroyed by e-beam exposure, as shown in the supplementary material (Fig. S3). Under high-energy e-beam irradiation, volatile Bi may evaporate, or the weak Bi–O bond may be susceptible to breakage.[29] To date, atomic-resolution TEM images of BBO have yet to be reported.

Instead of direct TEM studies, we performed first-principles calculations to examine the atomic arrangements of the BBO film on the non-breathing octahedral BCO layer. We used density functional theory (DFT) with the projector-augmented wave method, as implemented in the Vienna *Ab Initio* Simulation Package (VASP) code.[30,31] The plane-wave energy cutoff was set at 600 eV, and an 8×8×1 *k*-point mesh was used for a $\sqrt{2} \times \sqrt{2}$ slab. Here we will use the concept of oxygen displacement modes, which were already introduced earlier in Fig. 1(c). As shown in the top-most panel of Fig. 1(c), the oxygen ions move laterally (i.e., along [100] and [010]) in the bulk BiO_2 layer, resulting in an oxygen expanding-shrinking mode. The second top panel shows that the oxygen ions move vertically (i.e., along [001]) in the bulk BaO layer, resulting in an oxygen up-down mode. We determined the magnitude of oxygen displacement in each mode by comparing the atomic positions with those calculated for the 1 × 1 BBO slab, which does not have OBD due to the absence of neighboring octahedra. Figure 3(a) shows how the calculated magnitudes of oxygen displacement modes vary in

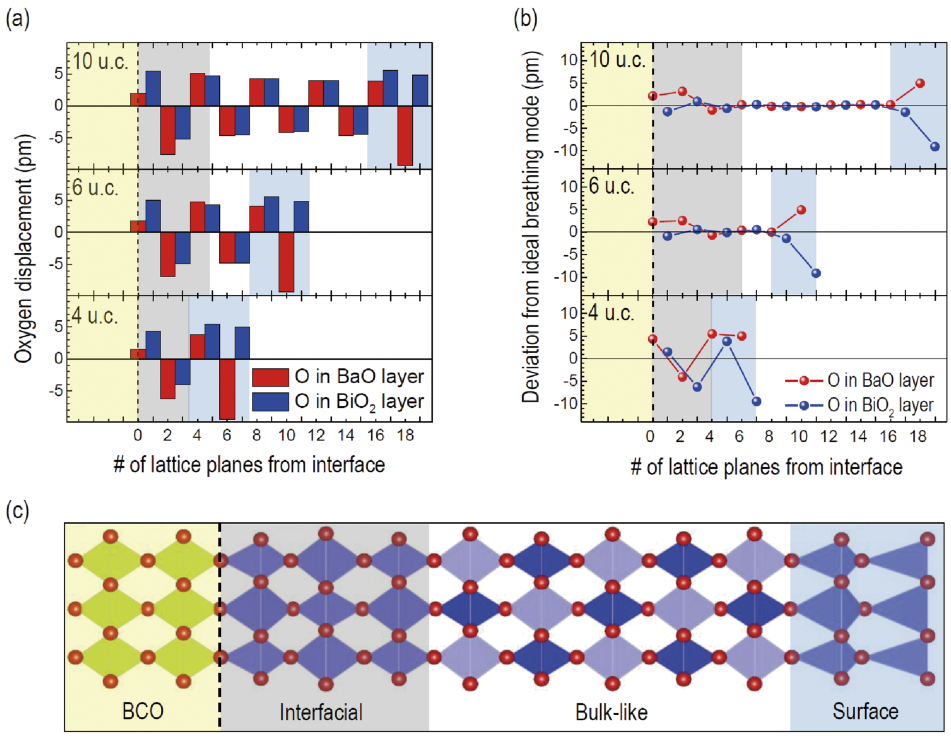

FIG. 3. (a) Calculated oxygen displacement in each unit cell of BBO with different lattice planes. The BCO sublayer is in the yellow background. At the BBO/BCO interface (gray-colored) and the BBO surface (blue-colored), the oxygen up-down mode in BaO slabs is broken while the change in the oxygen expanding-shrinking mode in BiO_2 slabs is negligible. To show our observation more intuitively, we display the oxygen displacement deviation from the ideal breathing mode, as shown in (b). The value 0 represents the ideal breathing pattern. (c) Schematic diagram of 10-u.c.-thick BBO on a BCO sublayer. The octahedral structure of BBO with three distinct regions is displayed in exaggerated scale.

terms of distance from the heterointerface. It may be easier to look at the deviation of the oxygen positions according to those of the ideal breathing mode. Thus, we converted the magnitudes of oxygen displacement modes into deviation from the OBD (with cubic A_{1g} symmetry) and plotted them in Fig. 3(b).

As shown schematically in Fig. 3(c), inside the BBO layer, there exist three distinct regions, which we refer to as interfacial, bulk-like, and surface regions. For example, consider the 10-u.c.-thick BBO film shown in Figs. 3(a) and 3(b). In the first three unit cells of the interfacial region (gray-colored), the oxygen up-down mode in the BaO slab becomes strongly suppressed in the first unit cell but enlarged in the second unit cell. In the bulk-like region (without any background color), residing at 3–7.5 u.c., oxygen displacement modes are close to those of the ideal OBD, namely, alternative oxygen displacements in either the BaO or BiO_2 slab. In the surface region (blue-colored), the oxygen up-down modes are enlarged, and expanding-shrinking modes are inverted in sign at the top layer, resulting in a huge deviation from ideal OBD. Note that the detailed structural relaxation of the oxygen cages at the interfacial and surface regions is significantly different.

Our calculations show the occurrence of anisotropic OBD suppression in the BBO layer. In the interfacial region, the oxygen up-down mode is suppressed at the first unit cell. However, there is no discernable change in the oxygen expanding-shrinking mode in the BiO_2 slab at the first unit cell. Notably, our experimental ellipsometry studies are sensitive to in-plane optical absorption. The remaining oxygen expanding-shrinking mode can explain the incomplete suppression of the 2-eV peak at 6 u.c., as shown in Fig. 2(b). In contrast, the Raman response should vanish immediately because anisotropic suppression of OBD breaks the A_{1g} symmetry completely. Note that the shape of octahedra in BBO cannot be arranged in the same geometry as that of non-breathing BCO. As a result, anisotropic distortion should occur in BBO due to different responses in each BaO layer and BiO_2 layer. Thus, a new type of octahedral distortion emerges at the heterointerface that is clearly different from OBD or the octahedra of BCO.

With a decrease in the BBO film thickness, the bulk-like region becomes monotonically smaller. However, the thicknesses of the interfacial and surface regions remain constant. Combining these two regions gives a correct critical thickness of OBD suppression of the BBO film. When the film was thinned below 6 u.c., most of the oxygen up-down modes deviated from those of the ideal breathing mode. In the 4 u.c. calculation results, displayed in Figs. 3(a) and 3(b), all of the OBD signatures are broken. These theoretical predictions are consistent with our experimentally observed value of critical thickness. In most oxide heterostructures, the critical thickness usually originates from interfacial effects, such as strain, intermixing, and electrostatic screening.[32–34] However, in our case of OBD suppression, both interfacial and surface effects were attributed to the critical thickness.

Numerous phenomena in nature are accompanied by oxygen breathing modes. For example, the importance of the dynamic oxygen breathing phonon modes has been pointed out in numerous high-T_c oxide superconductors, including cuprates[35–38] and bismuthates.[39,40] Static oxygen breathing distortions (i.e., OBD for the case of perovskite) are known to be concomitant with charge ordering.[41,42] When OBD is combined with other octahedral distortions, it generates a new ground state, such as orbital ordering with emerged Jahn–Teller distortion[41] and ferromagnetism with combined charge ordering and antiferromagnetic ordering.[43] Furthermore, as OBD in [111]-oriented bilayer perovskite can break the inversion symmetry, the emergence/suppression of new topological properties has been predicted.[44] To investigate such phenomena in perovskite oxide heterostructures, we should be aware of OBD suppression and relaxation at the interfaces. Furthermore, for the case where OBD suppression is required, we can archive the purpose via heterostructure engineering with the commensurate non-breathing sublayer.

In summary, we investigated OBD of fully strained BBO film responses at the heterointerface with a non-breathing layer. We observed that the OBD of BBO becomes suppressed at the commensurate heterointerface. A systematic method was established to interpret the OBD in terms of oxygen up-down and expanding-shrinking modes. We found that the OBD suppression is anisotropic due to the different responses of these two oxygen modes. This suppression occurs at both the heterointerface and the surface, resulting in a critical thickness value of 6 u.c.

See supplementary material for the characterizations of the samples with the X-ray diffraction, atomic force microscope, and transmission electron microscope.

This work was supported by the Research Center Program of IBS (Institute for Basic Science) in Korea (No. IBS-R009-D1). S.L. acknowledges support from DGIST start-up fund (No. 2018010054) and Basic Science Research Programs (No. NRF-2017R1C1B5018091) through the National Research Foundation of Korea.

[1] J. M. Rondinelli and N. A. Spaldin, Phys. Rev. B **82**, 113402 (2010).
[2] J. M. Rondinelli, S. J. May, and J. W. Freeland, MRS Bull. **37**, 261 (2012).
[3] J. B. Goodenough, Rep. Prog. Phys. **67**, 1915 (2004).
[4] H. W. Eng, P. W. Barnes, B. M. Auer, and P. M. Woodward, J. Solid State Chem. **175**, 94 (2003).
[5] H. Sato and M. Naito, Phys. C **274**, 221 (1997).
[6] W. Lu, W. Song, P. Yang, J. Ding, G. M. Chow, and J. Chen, Sci. Rep. **5**, 10245 (2015).
[7] K. J. Choi, Science **306**, 1005 (2004).
[8] J. Wang, J. B. Neaton, H. Zheng, V. Nagarajan, S. B. Ogale, B. Liu, D. Viehland, V. Vaithyanathan, D. G. Schlom, U.V. Waghmare, N. A. Spaldin, K. M. Rabe, M. Wuttig, and R. Ramesh, Science **299**, 1719 (2003).
[9] L. Qiao, J. H. Jang, D. J. Singh, Z. Gai, H. Xiao, A. Mehta, R. K. Vasudevan, A. Tselev, Z. Feng, H. Zhou, S. Li, W. Prellier, X. Zu, Z. Liu, A. Borisevich, A. P. Baddorf, and M. D. Biegalski, Nano Lett. **15**, 4677 (2015).
[10] J. He, A. Borisevich, S. V. Kalinin, S. J. Pennycook, and S. T. Pantelides, Phys. Rev. Lett. **105**, 227203 (2010).
[11] S. Catalano, M. Gibert, V. Bisogni, F. He, R. Sutarto, M. Viret, P. Zubko, R. Scherwitzl, G. A. Sawatzky, T. Schmitt, and J.-M. Triscone, APL Mater. **3**, 62506 (2015).
[12] A. Y. Borisevich, H. J. Chang, M. Huijben, M. P. Oxley, S. Okamoto, M. K. Niranjan, J. D. Burton, E. Y. Tsymbal, Y. H. Chu, P. Yu, R. Ramesh, S. V. Kalinin, and S. J. Pennycook, Phys. Rev. Lett. **105**, 87204 (2010).
[13] T. T. Fister, H. Zhou, Z. Luo, S. S. A. Seo, S. O. Hruszkewycz, D. L. Proffit, J. A. Eastman, P. H. Fuoss, P. M. Baldo, H. N. Lee, and D. D. Fong, APL Mater. **2**, 21102 (2014).
[14] J. M. Rondinelli and C. J. Fennie, Adv. Mater. **24**, 1961 (2012).
[15] S. J. May, C. R. Smith, J.-W. Kim, E. Karapetrova, A. Bhattacharya, and P. J. Ryan, Phys. Rev. B **83**, 153411 (2011).
[16] A. W. Sleight, Phys. C **514**, 152 (2015).
[17] K. Foyevtsova, A. Khazraie, I. Elfimov, and G. A. Sawatzky, Phys. Rev. B **91**, 121114 (2015).
[18] H. Sato, S. Tajima, H. Takagi, and S. Uchida, Nature **338**, 241 (1989).
[19] T. Nishio, J. Ahmad, and H. Uwe, Phys. Rev. Lett. **95**, 176403 (2005).
[20] A. W. Sleight, J. L. Gillson, and P. E. Bierstedt, Solid State Commun. **17**, 27 (1975).
[21] R. J. Cava, B. Batlogg, J. J. Krajewski, R. Farrow, L. W. Rupp, A. E. White, K. Short, W. F. Peck, and T. Kometani, Nature **332**, 814 (1988).
[22] S. Uchida, K. Kitazawa, and S. Tanaka, Phase Transitions **8**, 95 (1987).
[23] R. Jaramillo, S. D. Ha, D. M. Silevitch, and S. Ramanathan, Nat. Phys. **10**, 304 (2014).
[24] A. Subedi, O. E. Peil, and A. Georges, Phys. Rev. B **91**, 075128 (2015).
[25] H. G. Lee, Y. Kim, S. Hwang, G. Kim, T. D. Kang, M. Kim, M. Kim, and T. W. Noh, APL Mater. **4**, 126106 (2016).
[26] M. Kawasaki, T. Maeda, R. Tsuchiya, and H. Koinuma, Science **266**, 1540 (1993).
[27] S. Tajima, M. Yoshida, N. Koshizuka, H. Sato, and S. Uchida, Phys. Rev. B **46**, 1232 (1992).
[28] N. C. Plumb, D. J. Gawryluk, Y. Wang, Z. Ristić, J. Park, B. Q. Lv, Z. Wang, C. E. Matt, N. Xu, T. Shang, K. Conder, J. Mesot, S. Johnston, M. Shi, and M. Radović, Phys. Rev. Lett. **117**, 37002 (2016).
[29] P. Patnaik, *Handbook of Inorganic Chemical Compounds* (McGraw-Hill, 2003).
[30] G. Kresse and J. Furthmüller, Comput. Mater. Sci. **6**, 15 (1996).
[31] G. Kresse and J. Furthmüller, Phys. Rev. B **54**, 11169 (1996).
[32] J. Q. He, E. Vasco, C. L. Jia, and R. H. Wang, Appl. Phys. Lett. **87**, 62901 (2005).
[33] M. Cecot, L. Karwacki, W. Skowronski, J. Kanak, J. Wrona, A. Zywczak, L. Yao, S. van Dijken, J. Barnas, and T. Stobiecki, Sci. Rep. **7**, 968 (2017).
[34] M. Stengel and N. A. Spaldin, Nature **443**, 679 (2006).
[35] T. P. Devereaux, T. Cuk, Z. X. Shen, and N. Nagaosa, Phys. Rev. Lett. **93**, 117004 (2004).
[36] P. Piekarz, J. Konior, and J. H. Jefferson, Phys. Rev. B **59**, 697 (1999).
[37] P. Zhang, S. G. Louie, and M. L. Cohen, Phys. Rev. Lett. **98**, 67005 (2007).
[38] H. Iwasawa, J. F. Douglas, K. Sato, T. Masui, Y. Yoshida, Z. Sun, H. Eisaki, H. Bando, A. Ino, M. Arita, K. Shimada, H. Namatame, M. Taniguchi, S. Tajima, S. Uchida, T. Saitoh, D. S. Dessau, and Y. Aiura, Phys. Rev. Lett. **101**, 157005 (2008).
[39] Z. P. Yin, A. Kutepov, and G. Kotliar, Phys. Rev. X **3**, 21011 (2013).
[40] M. Braden, W. Reichardt, S. Shiryaev, and S. N. Barilo, Phys. C **378–381**, 89 (2002).
[41] P. V. Balachandran and J. M. Rondinelli, Phys. Rev. B **88**, 54101 (2013).
[42] L. Jiang, D. Saldana-Greco, J. T. Schick, and A. M. Rappe, Phys. Rev. B **89**, 235106 (2014).
[43] N. C. Bristowe, J. Varignon, D. Fontaine, E. Bousquet, and P. Ghosez, Nat. Commun. **6**, 6677 (2015).
[44] A. Rüegg, C. Mitra, A. A. Demkov, and G. A. Fiete, Phys. Rev. B **88**, 115146 (2013).